Dopant-Free Planar n-i-p Perovskite Solar Cells with Steady-State Efficiencies Exceeding 18%

Severin N. Habisreutinger[1]*, *Bernard Wenger*[1], *Henry J. Snaith*[1] & *Robin J. Nicholas*[1]*

[1] University of Oxford, Department of Physics, Clarendon Laboratory, Parks Road, Oxford OX1 3PU, United Kingdom

*habisreutinger@physics.ox.ac.uk

*robin.nicholas@physics.ox.ac.uk

ABSTRACT

In this letter we demonstrate a planar n-i-p perovskite solar cell design with a steady-state efficiency of up to 18.8% in the absence of any electronic dopants. In the device stack, solution-processed SnO_2 is used as electron-accepting n-type layer. The absorber layer is a perovskite with both mixed organic A-site cations and mixed halides ($FA_{0.83}MA_{0.17}Pb(I_{0.83}Br_{0.17})_3$). The hole-transporting p-type layer is a double-layer structure of polymer-wrapped single-walled carbon nanotubes and undoped spiro-OMeTAD. We show that this approach can deliver steady-state efficiencies as

high as and even higher than traditionally doped spiro-OMeTAD, providing a pathway for dopant-free perovskite solar cells crucial for long-term stability.

TOC Graphic

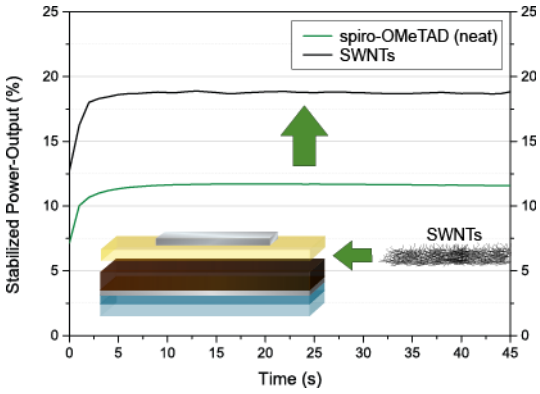

Halide perovskite solar cells continue to generate a lot of interest and enthusiasm among researchers, largely due to the prospect of readily transitioning from a purely lab based technology to real-world scales. This expectation is largely based on the rapid increase in efficiency over the past few years to values above 22%.[1] The next challenge will be to develop perovskite devices which can retain these efficiencies but in addition are stable for the long term.[1] This can be achieved by either developing a more stable perovskite absorber or by improving the device architecture such that the perovskite absorber is better protected from extrinsic degradation. Currently, the main body of research in the field has been focused on two architectures: the original n-i-p stack, where the transparent electrode collects electrons, and the p-i-n stack, where the charges travel in the opposite direction, and the transparent electrode collects the holes.[2] The efficiency of p-i-n devices has steadily increased in recent years to efficiencies up to 20%,[3] but thus far, the n-i-p stack has kept its edge, with efficiencies in the range of 21-22%.[4,5]

Essential components of this device architecture are the two charge selective contacts. The n-type contact in the majority of all devices is TiO_2, either in a planar configuration,[6] as a thin compact layer, or in a mesostructured configuration where an additional mesoporous layer of TiO_2 (150-300 nm) increases the contact area with the perovskite absorber.[4,5] To address the issue of non-steady state hysteresis effects,[7,8] interface modification of TiO_2 with ionic liquids[9] or fullerenes have been shown to have beneficial effects.[10] Extending this finding even further, TiO_2 was completely replaced by C_{60} derivatives as n-type contacts.[11,12] Recently, SnO_2 has moved into the spotlight as the n-type contact with recent studies reporting excellent steady-state performances.[13–16]

The p-type contact on the other side of the absorber has been investigated even more intensively.[17,18] The development of new materials has been focused on high-efficiencies but also on improved device stability.[1] Interestingly, however, the best-performing devices[5] still use the "original" hole-transport material 2,2,7,7-tetrakis-(N,N-di-p-methoxyphenylamine)9,9-spirobifluorene (spiro-OMeTAD), which had been the crucial ingredient for the breakthrough of the perovskite solar cell in 2012.[19,20] The fact that the amorphous hole-conductor spiro-OMeTAD performs as well as it does, is quite remarkable considering that it was conceived to mimic liquid electrolytes in dye-sensitized solar cells.[21] Its biggest flaw is that it is not sufficiently conductive for efficient charge-transport, and therefore requires extrinsic doping, which is typically done with Li-TFSI.[22,23] The biggest concern with regard to using Li-TFSI is that it is highly hygroscopic which has been shown to detrimentally impact the device stability due to accelerated moisture ingress.[24] There have been numerous efforts to either improve the inherent conductivity of spiro-OMeTAD by other means,[25,26] or to synthesize alternative hole-transporting materials which have an

inherently high hole-conductivity and therefore do not require additional doping.[18,27,28]

For a dopant-free n-i-p system, the highest reported scanned efficiency is 17.3% while the highest reported steady-state efficiency to date is around 15.0%.[28,29] In contrast, when spiro-OMeTAD is fully doped including Li-TFSI and the cobalt dopant FK9209, the currently highest steady-state performance in the literature is 21.6%.[5]

In this report, we demonstrate the effectiveness of using polymer-wrapped single-walled carbon nanotubes (SWNTs) as conductive elements in undoped spiro-OMeTAD to achieve a steady-state efficiency of up to 18.8%, exceeding the performance of the control devices with spiro-OMeTAD as hole-transport material, even those in which spiro-OMeTAD is conventionally doped with Li-TFSI.

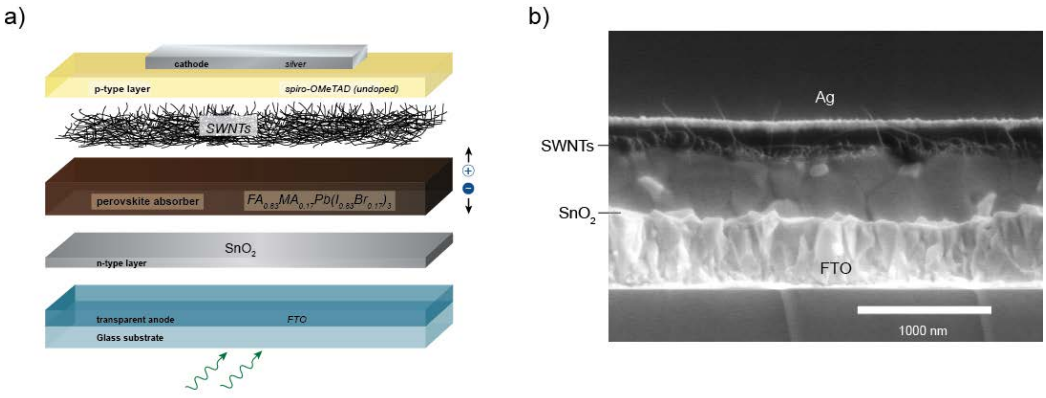

Figure 1: a) The transparent electrode is FTO (~7 Ohm/square) and collects electrons from the n-type contact, a solution-processed SnO_2 layer. The perovskite absorber is $FA_{0.83}MA_{0.17}Pb(I_{0.87}Br_{0.17})_3$. The p-type contact is formed by a dense multilayer of polymer-wrapped single-walled carbon nanotubes and a sequentially deposited layer of undoped spiro-OMeTAD. The hole-collecting top electrode is silver. b) The scanning-electron microscope

(SEM) image of a device cross-section, including the interlayer of SWNTs. The SWNTs are clearly visible protruding from the interface between the perovskite absorber and the undoped spiro-OMeTAD layer.

The device stack of this study is shown in Figure 1. The electron-collecting transparent electrode is made of fluorine-doped SnO_2. The n-type contact which blocks holes but collects photogenerated electrons from the perovskite is a planar SnO_2 layer which has been prepared according to Anaraki et al.[15] The perovskite absorber is the mixed absorber $FA_{0.83}MA_{0.17}Pb(I_{0.87}Br_{0.17})_3$ which has first been described by Jeon et al.[30] The p-type contact is formed by a polymer-wrapped single-walled carbon nanotube (SWNT) multilayer. For processing the SWNTs, they were wrapped in a monolayer of poly(3-hexylthiophene) (P3HT), the excess polymer which is not wrapped around SWNTs was removed prior to deposition.[31] After the deposition of the SWNTs, a layer of undoped spiro-OMeTAD is spin-coated on top, filling in the gaps in the SWNT mesh, thus preventing recombination losses at the metal electrode.

In Figure 1b, the scanning electron microscope (SEM) image of a device cross section is shown, of a device with the SWNT interlayer. At the interface between the perovskite absorber and the layer of undoped spiro-OMeTAD, the thin bright protruding filaments can be identified as the polymer wrapped SWNTs.

SWNTs, in contrast, to Li-TFSI are non-hygroscopic and do not directly react with spiro-OMeTAD. Instead, they form a network of high-mobility, conductive channels which selectively remove photogenerated holes from the perovskite interface, largely independent from the spiro-OMeTAD matrix.[24,26] To demonstrate their impact on device performance, two types of control devices were prepared: one with just undoped, neat spiro-OMeTAD, and one with doped spiro-OMeTAD as p-type

contact. The doping was done with lithium bis(trifluoromethylsulfonyl)imide (Li-TFSI) with the concentrations of the currently highest published efficiency devices.[5] All three device structures contain 4-*tert*-butylpyridine (*t*BP), which we have shown in a previous study to directly interact with the perovskite making the interface with the HTM more p-type, thus inducing beneficial band bending which significantly enhances the steady-state charge extraction.[32]

We show the current-voltage characteristics of the reverse scans (Figure 2a) and the stabilized power output (SPO) (Figure 2b) – a metric for the steady-state efficiency – of the best-performing devices for all three configurations. The performance parameters are summarized in Table 1, the corresponding device statistics are shown in Figure 2c and 2d.

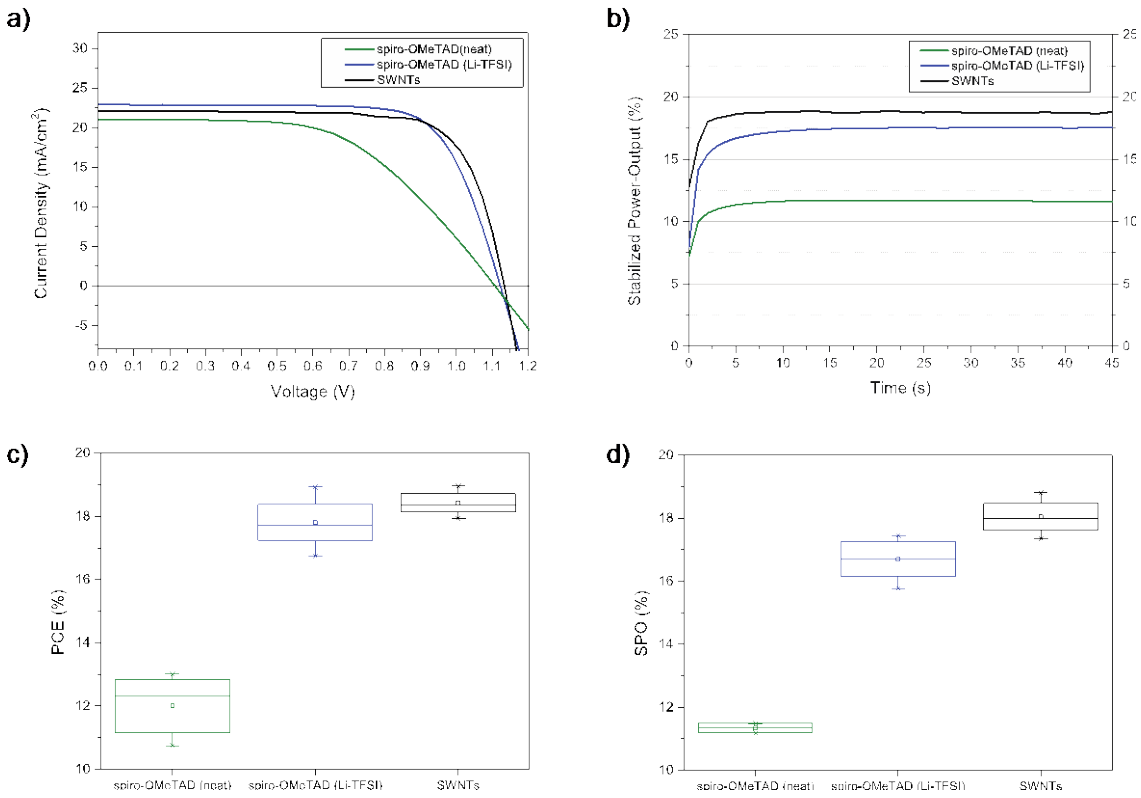

Figure 2: a) Current-voltage curves of the reverse scans for the best performing devices with neat spiro-OMetAD, doped spiro-OMeTAD and SWNTs. b) Stabilized power output obtained from photocurrent tracking at the maximum power-point voltage (corresponding to the transient current-

voltage sweeps in a)). The device statistics (30 devices) of the scanned power-conversion efficiency are shown in c), and the corresponding stabilized power-output values are shown in d).

In the device stack in which the hole-transport material spiro-OMeTAD is undoped, the impact of the very low conductivity of the amorphous material becomes apparent in the form of a dominating series resistance (15.6 $\Omega \cdot cm^2$) which limits the overall efficiency to around 12.7%. Although it has been shown that the hole mobility of neat spiro-OMeTAD increases from 10^{-5} to close to 10^{-3} cm^2 $V^{-1}s^{-1}$ under light,[33] this is, however, still too low to match the hole mobility of Li-TFSI doped spiro-OMeTAD. This can be seen in the current-voltage curve of the device with the doped HTM. The improvement in the efficiency to 18.7% results from a slightly enhanced charge extraction, but mainly from a significantly larger fill factor due to the much lower series resistance (5.7 $\Omega \cdot cm^2$). Similarly, when the SWNTs are deposited at the interface between the perovskite absorber and an undoped spiro-OMeTAD layer, the series resistance is further reduced (2.3 $\Omega \cdot cm^2$), leading to a fill factor of 0.75, which combined with a short-circuit current of 22.07 mA cm^{-2} and an open-circuit voltage of 1.14 V, yields a power-conversion efficiency of 18.9%. The current-voltage curves are very useful to identify macroscopic limitations within a device structure, as in this case, where we can clearly point to the series resistance as the limiting factor for the poorly conductive neat spiro-OMeTAD layer. The peculiar characteristic of perovskite solar cells that the JV-curve is affected by the scanning conditions such as direction, speed and pre-biasing which makes JV-scans a poor metric for the operational efficiency of a photovoltaic device because the time scale of the scans often exceeds the time scale of the underlying transient processes responsible for this behavior.[7,34] As a means to avoid ambiguity and the risk of overestimating the actual

power-output capacity of a device, we hold it at its maximum power-point voltage (V_{MPP}) and let the photocurrent stabilize. As a result we obtain the stabilized power output (SPO) of a device which can serve as an unambiguous metric for the steady-state efficiency at which a solar cell would operate.[7,35]

The photocurrent tracking at V_{MPP} to obtain the SPO values are shown in Figure 2b. The SPOs for the neat and the doped spiro-OMeTAD device are 11.6% and 17.6%, respectively, showing a slight decrease compared to the scanned PCE values. In contrast, the SPO of 18.8% for the SWNT device matches its scanned PCE. We attribute the fact that charge extraction under steady-state conditions does not appear to be impacted by either trap assisted recombination,[36] ionic drift[34,37] or a combination of the two,[38] to the SWNTs forming an excellent interface with the perovskite due to a beneficial alignment of the energy levels which allows an efficient barrier-free extraction of photogenerated holes.[39,40]

Table 1: performance parameters of the best-performing devices with the three investigated different hole transport layers.

HTL architecture	J_{sc} [mA/cm^2]	V_{oc} [V]	FF	PCE [%]	SPO[%]	SPO/PCE
spiro-OMeTAD (neat)	21.02	1.11	0.55	12.7	**11.6**	0.92
spiro-OMeTAD (Li-TFSI)	22.89	1.12	0.73	18.7	**17.6**	0.94
SWNTs	22.07	1.14	0.75	18.9	**18.8**	1.00

To provide further insight into the underlying mechanism for the performance enhancements due to the presence of the SWNTs at the interface, we carried out steady-state photoluminescence (PL) and time-resolve photoluminescence (TRPL) measurements on the three investigated hole-transporter configurations, as well as on a bare perovskite layer (Figure 3). All samples were fabricated on glass substrates so that exclusively hole extraction could occur.

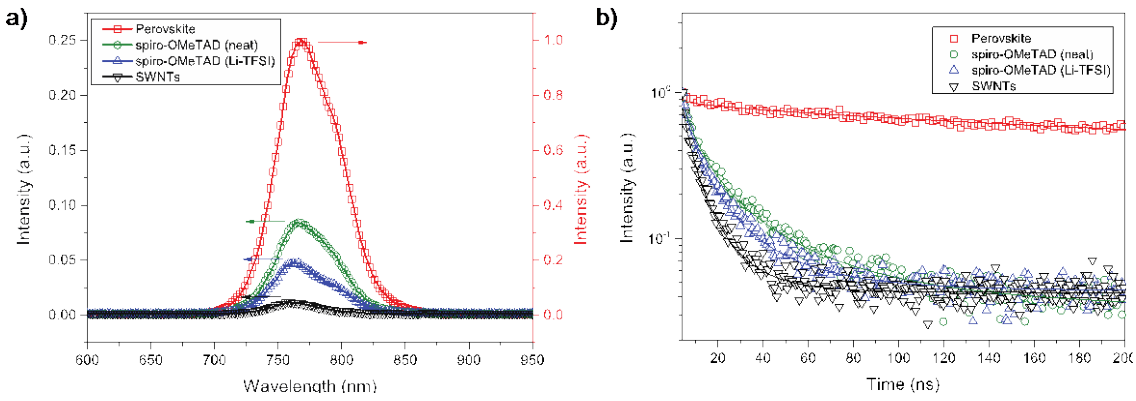

Figure 3: a) Normalized steady-state photoluminescence spectra at an excitation at 510 nm at the same fluence comparing the three hole-transporter layers to a perovskite without hole-transporter (red squares). b) Time-resolved photoluminescence spectra in the first 200 ns. The decay was fitted with a stretched exponential function (Table 2).

The characteristic PL peak for the bare perovskite layer is centered around 775 nm. For the films including a hole-transport layer this emission feature is significantly reduced, since some of the photogenerated holes are now transferred from the perovskite to the HTL and cannot recombine radiatively in the absorber. The magnitude of its reduction is attributed to the number of charges transferred to the HTL and thus removed from the population of radiatively recombining charge carriers.

Consistent with the device performance, this emission peak is further reduced by the presence of the SWNTs compared to the device without the nanotubes (Figure 3a), indicating a more effective extraction of holes by the SWNTs. At the same time, the PL lifetime is greatly reduced by the SWNTs, as shown in the time-resolved decay measurements (Figure 3b). These measurements are an indirect measure for the charge-carrier extraction dynamics at this interface.

Photoluminescence decay dynamics are determined by several pathways of radiative and non-radiative recombination, which can be identified by different decay features in the time-resolved traces (Figure 3b). In the presence of a hole-transporting material, selective carrier extraction adds another non-radiative pathway. The dynamics of charge extraction are complex and include charge transport and transfer through the interface which compete namely with radiative and trap-assisted recombination. To quantify semi-empirically the carrier lifetimes, we fit the experimental photoluminescence decays with a stretched exponential function,

$$f(\mathrm{t}) = A \cdot \mathrm{e}^{-(\mathrm{t}/\tau)^{\beta}}$$

in which $0 < \beta < 1$ is the stretch parameter and serves as an indicator of how the curve deviates from a single exponential decay ($\beta = 1$). The mean lifetime of the photogenerated charges $\langle\tau\rangle$ is given by :

$$\langle\tau\rangle = \int_0^{\infty} dt\ \mathrm{e}^{-(\mathrm{t}/\tau)^{\beta}} = \frac{\tau}{\beta}\,\Gamma\left(\frac{1}{\beta}\right)$$

where Γ is the gamma-function. The stretch parameter β and the calculated mean carrier lifetime τ are shown in Table 2.

Table 2: performance parameters of the best-performing devices with the three investigated different hole transport layers.

HTL architecture	$\langle\tau\rangle$ [ns]	β
Perovskite	725.8	0.67
spiro-OMeTAD (neat)	3.7	0.35
spiro-OMeTAD (Li-TFSI)	2.8	0.41
SWNTs	2.2	0.47

For all three dedicated hole transport layers, the mean carrier lifetime is reduced by more than two orders of magnitude compared to the perovskite layer without charge-selective contact. We measure the shortest carrier lifetime of around 2.2 ns for the SWNTs, which indicates that the photogenerated holes are most rapidly extracted in the presence of the SWNTs. Alternatively, photogenerated charges could recombine non-radiatively at the perovskite-SWNT interface, and thus be lost for radiative emission. However, the comparatively high open-circuit voltage in the full device suggests that this loss mechanism does not dominate the charge carrier dynamics at this interface. Instead, in agreement with previous ultrafast transient absorption measurements,[40] the SWNTs are able to both selectively and effectively extract holes on a very fast time scale.

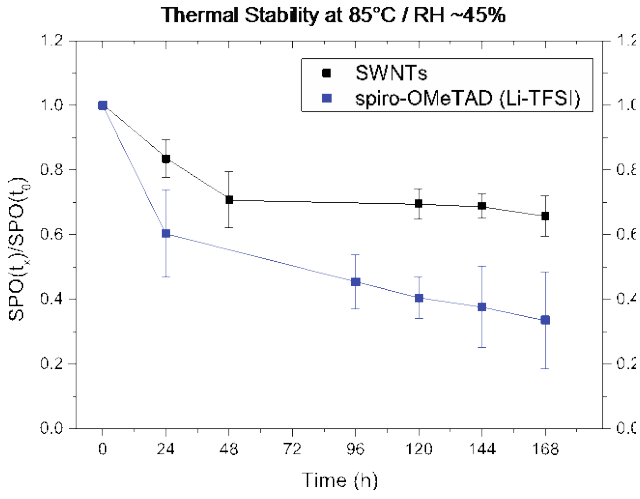

Figure 4: Thermal stress test of devices with doped spiro-OMeTAD and the SWNT-interlayer without dopant. The devices were exposed to 85°C in the dark at a relative humidity (RH) of ~45%. Each data point represents the average SPO(t_x) of 20 devices normalized by their initial SPO(t_0) prior to heat exposure.

In Figure 4, we show an initial demonstration of the increase in stability due to the absence of Li-TFSI as dopant. Devices with doped spiro-OMeTAD (Li-TFSI) and

devices with the SWNT-interlayer without the dopant were stress-tested at 85°C in the dark at a relative humidity (RH) ~45%. The data points represent the average SPO(t_x) of the device batch of at time t_x normalized by the initial SPO(t_0) prior to the thermal stress testing.

We attribute the initial drop in performance over the first 48h to the morphological instability of spiro-OMeTAD at elevated temperatures.[41] Malinauskas et al. show in in their study that the amorphous state of spiro-OMeTAD is not very stable and crystallization of the material may occur at elevated temperatures.[41] This change in morphology, they show, leads to a significant deterioration of the solar cell performance.

In our case, the formation of crystalline domains in the spiro-OMeTAD layer might also impact the contact of the SWNTs with their interfaces, thus being largely responsible for the initial decrease in performance (Figure 4). The additional significant decrease in device performance of the doped spiro-OMeTAD layer is attributed to an accelerated degradation of the absorber itself due to the presence of Li-TFSI. As a result, the device performance of devices with doped spiro-OMeTAD has decreased twice as much than that of devices with the SWNT-interlayer. However, our study illustrates further that spiro-OMeTAD, even in the absence of dopants, is not a particularly suitable hole-transporting material for long-term device stability likely due to its morphological instability.

In summary, we have demonstrated that polymer-wrapped nanotubes can be employed as a conductive element to improve the charge transport characteristics of neat spiro-OMeTAD in perovskite devices with $FA_{0.83}MA_{0.117}Pb(I_{0.87}Br_{0.17})_3$ as absorber to achieve a scanned power-conversion efficiency of up to 18.8%. More

importantly, the corresponding steady-state efficiency matches this value, demonstrating that this hole-transporter system can yield devices which are not negatively affected by current-voltage hysteresis. In comparison, the control device with fully doped spiro-OMeTAD yielded a scanned efficiency of 18.7% but showed a reduced stabilized efficiency of 17.6%. With this we have expanded the arsenal of hole-transporter systems for high-performance perovskite devices which deliver a high power-conversion efficiency without requiring any hygroscopic dopants, which has significant implications for long-term device stability.

EXPERIMENTAL METHODS

SWNT Functionalization.

Powdered singled-walled carbon nanotubes (SWNTs) produced by the CoMoCAT process, SWeNT CG200, were purchased from Sigma Aldrich. They have a diameter range from 0.7−1.4 nm and a relative purity of 90% as the percentage of carbon that is present as SWNTs. 3.0 mg of rr-P3HT (Rieke Metals Inc., weight-average molecular weight, Mw = 50 000 g mol^{-1} and regioregularity = 95%) was dissolved in 5.00 mL of chlorobenzene and sonicated in a bath sonicator for 60 min. 2.5 mg of SWNTs were added, as purchased, to the dissolved polymer solution and treated with an ultrasonic probe for 10 min. After the sonication treatment 5 ml of chlorobenzene were added to improve the solubility of the polymer-nanotube-hybrids. The mixture was subsequently centrifuged for 8 min at 10 000g to remove non-functionalized SWNTs and other carbonaceous particles. The precipitate was discarded while the supernatant was recovered. In order to remove the excess polymer according to the

solvent extraction technique detailed by Schuettfort et al.,[42] 10 mL of toluene was added. The mixture was then mildly heated for 60 min to induce aggregation of the functionalized SWNTs. The aggregates were then removed by centrifugation (4 min at 16 000 g). The supernatant containing excess polymer was discarded and the precipitate was recovered. The pellet consists of 1.5−1.6 mg of polymer-wrapped nanotubes, which are dispersed in 6 mL of chloroform. Immediately prior to spin-coating, the chloroform dispersion was sonicated with an ultrasonic probe for 1 min at low intensity (∼10% of amplitude) to break up clusters and bundles.

Solar Cell Fabrication. A glass wafer with a layer of fluorine doped tin oxide (FTO) (TEC7) was first cleaned with detergent and de-ionized water, and then washed with ethanol. Thereafter it was treated for 5 min in O_2 plasma. The electron accepting SnO_2 was prepared in a two-step deposition first introduced by Anaraki et al.[15] For the first layer, tin(IV)chloride pentahydrate ($SnCl_4 \cdot 5H_2O$) (Sigma-Aldrich) was dissolved in 2-propanol 0.05 M and let stir for 30 min. The solution was spincoated at 3000 rpm for 30 s, with a ramp of 300 rpm/s. The substrates were then dried at 100°C for 10 min and annealed at 180°C for 60 min. For the second step, a chemical bath was prepared by dissolving tin(II) chloride dihydrate ($SnCl_2 \cdot 2H_2O$) (Sigma-Aldrich) in de-ionized water (DI-H_2O) 0.012 M together with 20.7 mM urea (Sigma-Aldrich) in addition to 0.15 M hydrochloric acid (Fisher scientific) and 2.87 μM 3-mercaptopropionic acid (Sigma-Aldrich). The substrates were immersed in the solution and kept at 70°C for 180 min. Afterwards, the substrates were washed with DI-H_2O and sonicated in a bath sonicator for 2 min in DI-H_2O. Thereafter, they were washed with ethanol and annealed at 180°C for 60 min. For mixed perovskite precursor 1.25 M formamidinium iodide (Dyesol), 0.25 M methylammonium bromide (Dyesol), 0.25 M lead bromide (Alfa Aesar), 1.375 M lead iodide (TCI) were

dissolved in a solvent mixture of *N*,*N*-dimethyformamide (DMF) and *N*,*N*-dimethyl sulfoxide (DMSO) (4:1 by volume), and stirred for 15 min at 65°C. The perovskite deposition was done in a drybox with a relative humidity of approximately 10%. For the deposition, 20 µl of the precursor solution were spincoated per substrate in a two-step process, spinning for 10 s at 1000 rpm and 35 s at 6000 rpm. 10 s before the end of the second spincoating step, the spinning substrate was quenched with 80 µl anisole (Sigma-Aldrich). Thereafter the perovskite films were annealed at 100°C in an oven.

For the hole-transport layer 85 mg/ml of 2,20,7,70-tetrakis-(N,N-di-p-methoxyphenyl-amine)9,9-spirobifluorene (Lumtec) were dissolved in chlorobenzene (Sigma-Aldrich), to which 33 µl/ml of 4-*tert*-butylpyridine (Sigma-Aldrich) were added. For the Li-TFSI doped control devices, 500 mg/ml lithium bis(tri-fluoromethanesulfonyl)imide (Sigma-Aldrich were dissolved in 1-butanol (Sigma-Aldrich), of which 20 µl/ml were added to the spiro-OMeTAD solution. The doped and undoped spiro-OMeTAD layer were deposited by spincoating at 2000 rpm for 45 s. The SWNTs were deposited dynamically by drop-by-drop spin-coating (3000 rpm for 90 s) of 200 µl of the SWNT dispersion. The film was blow-dried with an airgun and let sit to dry at RT for 15 min. Finally, silver electrodes were thermally evaporated onto the HTL.

Current-Voltage Measurements. For measuring the performance of the solar cells, simulated AM 1.5 sunlight was generated with a class AAB ABET solar simulator calibrated to give simulated AM 1.5, of 100.0 mW cm^{-2} equivalent irradiance, using an NREL-calibrated KG5 filtered silicon reference cel . The current-voltage curves were recorded with a sourcemeter (Keithley 2400, USA). The solar cells were masked with a metal aperture defining the active area (0.0919 cm^2) of the solar cells.

Additionally, by removing active material between individual cells on the same glass substrate, single-cell contributions were ensured. Measurements were done in a light-tight sample holder to minimize any edge effects and ensure that the reference cell and test cell are located during measurement in the same spot under the solar simulator.

Photoluminescence spectroscopy. Time-resolved PL decays were acquired using a time-correlated single photon counting (TCSPC) setup (FluoTime 300, PicoQuant GmbH). Samples were photoexcited using a 507 nm laser head (LDH-P-C-510, PicoQuant GmbH) with pulse duration of 117 ps, fluences of ~0.03 – 3 µJ/cm2/pulse, and a repetition rate of 0.1 to 1 MHz.

AUTHOR INFORMATION

Corresponding authors:

*habisreutinger@physics.ox.ac.uk

*robin.nicholas@physics.ox.ac.uk

Notes

The authors declare no competing financial interest.

ACKNOWLEDGEMENTS

The international Collaborative Energy Technology R&D Program of the Korean Institute of Energy Technology Evaluation and Planning (KETEP) with financial resource from the Ministry of Trade, Industry & Energy, Republic of Korea (no. 20148520011250), and by the EPSRC.

363 REFERENCES

364

365 (1) Habisreutinger, S. N.; McMeekin, D. P.; Snaith, H. J.; Nicholas, R. J. Research
366 Update: Strategies for Improving the Stability of Perovskite Solar Cells. *APL*
367 *Mater.* **2016**, *4* (9), 91503.
368 (2) Snaith, H. J. Perovskites: The Emergence of a New Era for Low-Cost, High-
369 Efficiency Solar Cells. *J. Phys. Chem. Lett.* **2013**, 3623–3630.
370 (3) Zhao, J.; Zheng, X.; Deng, Y.; Li, T.; Shao, Y.; Gruverman, A.; Shield, J.;
371 Huang, J. Is Cu a Stable Electrode Material in Hybrid Perovskite Solar Cells
372 for a 30-Year Lifetime? *Energy Environ. Sci.* **2016**, *9* (12), 3650–3656.
373 (4) Saliba, M.; Matsui, T.; Seo, J.-Y.; Domanski, K.; Correa-Baena, J.-P.;
374 Nazeeruddin, M. K.; Zakeeruddin, S. M.; Tress, W.; Abate, A.; Hagfeldt, A.; et
375 al. Cesium-Containing Triple Cation Perovskite Solar Cells: Improved
376 Stability, Reproducibility and High Efficiency. *Energy Environ. Sci.* **2016**, *9*
377 (6), 1989–1997.
378 (5) Saliba, M.; Matsui, T.; Domanski, K.; Seo, J.-Y.; Ummadisingu, A.;
379 Zakeeruddin, S. M.; Correa-Baena, J.-P.; Tress, W. R.; Abate, A.; Hagfeldt, A.;
380 et al. Incorporation of Rubidium Cations into Perovskite Solar Cells Improves
381 Photovoltaic Performance. *Science* **2016**, *354* (6309), 206–209.
382 (6) Eperon, G. E.; Burlakov, V. M.; Docampo, P.; Goriely, A.; Snaith, H. J.
383 Morphological Control for High Performance, Solution-Processed Planar
384 Heterojunction Perovskite Solar Cells. *Adv. Funct. Mater.* **2014**, *24* (1), 151–
385 157.
386 (7) Snaith, H. J.; Abate, A.; Ball, J. M.; Eperon, G. E.; Leijtens, T.; Noel, N. K.;
387 Stranks, S. D.; Wang, J. T.-W.; Wojciechowski, K.; Zhang, W. Anomalous

Hysteresis in Perovskite Solar Cells. *J. Phys. Chem. Lett.* **2014**, *5* (9), 1511–1515.

(8) Unger, E. L.; Hoke, E. T.; Bailie, C. D.; Nguyen, W. H.; Bowring, A. R.; Heumuller, T.; Christoforo, M. G.; McGehee, M. D. Hysteresis and Transient Behavior in Current-Voltage Measurements of Hybrid-Perovskite Absorber Solar Cells. *Energy Environ. Sci.* **2014**, *7*, 3690–3698.

(9) Yang, D.; Zhou, X.; Yang, R.; Yang, Z.; Yu, W.; Wang, X.; Li, C.; Liu, S. F.; Chang, R. P. H. Surface Optimization to Eliminate Hysteresis for Record Efficiency Planar Perovskite Solar Cells. *Energy Environ. Sci.* **2016**, *9* (10), 3071–3078.

(10) Wojciechowski, K.; Stranks, S. D.; Abate, A.; Sadoughi, G.; Sadhanala, A.; Kopidakis, N.; Rumbles, G.; Li, C.; Friend, R. H.; Jen, A. K.-Y.; et al. Heterojunction Modification for Highly Efficient Organic–Inorganic Perovskite Solar Cells. *ACS Nano* **2014**, *8* (12), 12701–12709.

(11) Wojciechowski, K.; Leijtens, T.; Siprova, S.; Schlueter, C.; Hörantner, M. T.; Wang, J. T. W.; Li, C. Z.; Jen, A. K. Y.; Lee, T. L.; Snaith, H. J. C_{60} as an Efficient n-Type Compact Layer in Perovskite Solar Cells. *J. Phys. Chem. Lett.* **2015**, *6* (12), 2399–2405.

(12) Wojciechowski, K.; Ramirez, I.; Gorisse, T.; Dautel, O.; Dasari, R.; Sakai, N.; Hardigree, J. M.; Song, S.; Marder, S.; Riede, M.; et al. Cross-Linkable Fullerene Derivatives for Solution-Processed n–i–p Perovskite Solar Cells. *ACS Energy Lett.* **2016**, *1* (4), 648–653.

(13) Correa Baena, J. P.; Steier, L.; Tress, W.; Saliba, M.; Neutzner, S.; Matsui, T.; Giordano, F.; Jacobsson, T. J.; Srimath Kandada, A. R.; Zakeeruddin, S. M.; et al. Highly Efficient Planar Perovskite Solar Cells Through Band Alignment

Engineering. *Energy Environ. Sci.* **2015**, *8* (10), 2928–2934.

(14) Ke, W.; Zhao, D.; Xiao, C.; Wang, C.; Cimaroli, A. J.; Grice, C. R.; Yang, M.; Li, Z.; Jiang, C.-S.; Al-Jassim, M.; et al. Cooperative Tin Oxide Fullerene Electron Selective Layers for High-Performance Planar Perovskite Solar Cells. *J. Mater. Chem. A* **2016**, *4* (37), 14276–14283.

(15) Anaraki, E. H.; Kermanpur, A.; Steier, L.; Domanski, K.; Matsui, T.; Tress, W.; Saliba, M.; Abate, A.; Grätzel, M.; Hagfeldt, A.; et al. Highly Efficient and Stable Planar Perovskite Solar Cells by Solution-Processed Tin Oxide. *Energy Environ. Sci.* **2016**, *9* (10), 3128–3134.

(16) McMeekin, D. P.; Sadoughi, G.; Rehman, W.; Eperon, G. E.; Saliba, M.; Horantner, M. T.; Haghighirad, A.; Sakai, N.; Korte, L.; Rech, B.; et al. A Mixed-Cation Lead Mixed-Halide Perovskite Absorber for Tandem Solar Cells. *Science* **2016**, *351* (6269), 151–155.

(17) Yu, Z.; Sun, L. Recent Progress on Hole-Transporting Materials for Emerging Organometal Halide Perovskite Solar Cells. *Adv. Energy Mater.* **2015**, *5* (12), 1500213.

(18) Calió, L.; Kazim, S.; Grätzel, M.; Ahmad, S. Hole-Transport Materials for Perovskite Solar Cells. *Angew. Chemie Int. Ed.* **2016**, *55* (47), 14522–14545.

(19) Lee, M. M.; Teuscher, J.; Miyasaka, T.; Murakami, T. N.; Snaith, H. J. Efficient Hybrid Solar Cells Based on Meso-Superstructured Organometal Halide Perovskites. *Science* **2012**, *338* (6107), 643–647.

(20) Kim, H.-S.; Lee, C.-R.; Im, J.-H.; Lee, K.-B.; Moehl, T.; Marchioro, A.; Moon, S.-J.; Humphry-Baker, R.; Yum, J.-H.; Moser, J. E.; et al. Lead Iodide Perovskite Sensitized All-Solid-State Submicron Thin Film Mesoscopic Solar Cell with Efficiency Exceeding 9%. *Sci. Rep.* **2012**, *2*, 591.

(21) Bach, U.; Lupo, D.; Comte, P.; Moser, J. E.; Weissörtel, F.; Salbeck, J.; Spreitzer, H.; Grätzel, M. Solid-State Dye-Sensitized Mesoporous TiO_2 Solar Cells with High Photon-to-Electron Conversion Efficiencies. *Nature* **1998**, *395* (6702), 583–585.

(22) Snaith, H. J.; Grätzel, M. Enhanced Charge Mobility in a Molecular Hole Transporter via Addition of Redox Inactive Ionic Dopant: Implication to Dye-Sensitized Solar Cells. *Appl. Phys. Lett.* **2006**, *89* (26), 262114.

(23) Abate, A.; Leijtens, T.; Pathak, S.; Teuscher, J.; Avolio, R.; Errico, M. E.; Kirkpatrik, J.; Ball, J. M.; Docampo, P.; McPherson, I.; et al. Lithium Salts as "Redox Active" p-Type Dopants for Organic Semiconductors and Their Impact in Solid-State Dye-Sensitized Solar Cells. *Phys. Chem. Chem. Phys.* **2013**, *15* (7), 2572–2579.

(24) Habisreutinger, S. N.; Leijtens, T.; Eperon, G. E.; Stranks, S. D.; Nicholas, R. J.; Snaith, H. J. Carbon Nanotube/Polymer Composites as a Highly Stable Hole Collection Layer in Perovskite Solar Cells. *Nano Lett.* **2014**, *14* (10), 5561–5568.

(25) Nguyen, W. H.; Bailie, C. D.; Unger, E. L.; McGehee, M. D. Enhancing the Hole-Conductivity of Spiro-OMeTAD Without Oxygen or Lithium Salts by Using $Spiro(TFSI)_2$ in Perovskite and Dye-Sensitized Solar Cells. *J. Am. Chem. Soc.* **2014**, *136* (31), 10996–11001.

(26) Habisreutinger, S. N.; Leijtens, T.; Eperon, G. E.; Stranks, S. D.; Nicholas, R. J.; Snaith, H. J. Enhanced Hole Extraction in Perovskite Solar Cells Through Carbon Nanotubes. *J. Phys. Chem. Lett.* **2014**, *5*, 4207–4212.

(27) Liu, J.; Wu, Y.; Qin, C.; Yang, X.; Yasuda, T.; Islam, A.; Zhang, K.; Peng, W.; Chen, W.; Han, L. A Dopant-Free Hole-Transporting Material for Efficient and

Stable Perovskite Solar Cells. *Energy Environ. Sci.* **2014**, *7* (9), 2963–2967.

(28) Kim, G.-W.; Kang, G.; Kim, J.; Lee, G.-Y.; Kim, H. Il; Pyeon, L.; Lee, J.; Park, T. Dopant-Free Polymeric Hole Transport Materials for Highly Efficient and Stable Perovskite Solar Cells. *Energy Environ. Sci.* **2016**, *9* (7), 2326–2333.

(29) Liu, Y.; Hong, Z.; Chen, Q.; Chen, H.; Chang, W.-H.; Yang, Y. M.; Song, T.-B.; Yang, Y. Perovskite Solar Cells Employing Dopant-Free Organic Hole Transport Materials with Tunable Energy Levels. *Adv. Mater.* **2016**, *28* (3), 440–446.

(30) Jeon, N. J.; Noh, J. H.; Yang, W. S.; Kim, Y. C.; Ryu, S.; Seo, J.; Seok, S. Il. Compositional Engineering of Perovskite Materials for High-Performance Solar Cells. *Nature* **2015**, *517* (7535), 476–480.

(31) Schuettfort, T.; Nish, A.; Nicholas, R. J. Observation of a Type II Heterojunction in a Highly Ordered Polymer−Carbon Nanotube Nanohybrid Structure. *Nano Lett.* **2009**, *9* (11), 3871–3876.

(32) Habisreutinger, S. N.; Noel, N. K.; Snaith, H. J.; Nicholas, R. J. Investigating the Role of 4-Tert Butylpyridine in Perovskite Solar Cells. *Adv. Energy Mater.* **2016**, 1601079.

(33) Leijtens, T.; Lim, J.; Teuscher, J.; Park, T.; Snaith, H. J. Charge Density Dependent Mobility of Organic Hole-Transporters and Mesoporous TiO_2 Determined by Transient Mobility Spectroscopy: Implications to Dye-Sensitized and Organic Solar Cells. *Adv. Mater.* **2013**, *25* (23), 3227–3233.

(34) Tress, W.; Marinova, N.; Moehl, T.; Zakeeruddin, S. M.; Nazeeruddin, M. K.; Grätzel, M. Understanding the Rate-Dependent J–V Hysteresis, Slow Time Component, and Aging in $CH_3NH_3PbI_3$ Perovskite Solar Cells: The Role of a

Compensated Electric Field. *Energy Environ. Sci.* **2015**, *8* (3), 995–1004.

(35) Zimmermann, E.; Wong, K. K.; Müller, M.; Hu, H.; Ehrenreich, P.; Kohlstädt, M.; Würfel, U.; Mastroianni, S.; Mathiazhagan, G.; Hinsch, A.; et al. Characterization of Perovskite Solar Cells: Towards a Reliable Measurement Protocol. *APL Mater.* **2016**, *4* (9).

(36) Noel, N. K.; Abate, A.; Stranks, S. D.; Parrott, E. S.; Burlakov, V. M.; Goriely, A.; Snaith, H. J. Enhanced Photoluminescence and Solar Cell Performance via Lewis Base Passivation of Organic–Inorganic Lead Halide Perovskites. *ACS Nano* **2014**, *8* (10), 9815–9821.

(37) Eames, C.; Frost, J. M.; Barnes, P. R. F.; O'Regan, B. C.; Walsh, A.; Islam, M. S. Ionic Transport in Hybrid Lead Iodide Perovskite Solar Cells. *Nat. Commun.* **2015**, *6*, 7497.

(38) van Reenen, S.; Kemerink, M.; Snaith, H. J. Modeling Anomalous Hysteresis in Perovskite Solar Cells. *J. Phys. Chem. Lett.* **2015**, *6* (19), 3808–3814.

(39) Schulz, P.; Dowgiallo, A.-M.; Yang, M.; Zhu, K.; Blackburn, J. L.; Berry, J. J. Charge Transfer Dynamics between Carbon Nanotubes and Hybrid Organic Metal Halide Perovskite Films. *J. Phys. Chem. Lett.* **2016**, *7* (3), 418–425.

(40) Ihly, R.; Dowgiallo, A.-M.; Yang, M.; Schulz, P.; Stanton, N. J.; Reid, O. G.; Ferguson, A. J.; Zhu, K.; Berry, J. J.; Blackburn, J. L. Efficient Charge Extraction and Slow Recombination in Organic-Inorganic Perovskites Capped with Semiconducting Single-Walled Carbon Nanotubes. *Energy Environ. Sci.* **2016**, *9* (4), 1439–1449.

(41) Malinauskas, T.; Tomkute-Luksiene, D.; Sens, R.; Daskeviciene, M.; Send, R.; Wonneberger, H.; Jankauskas, V.; Bruder, I.; Getautis, V. Enhancing Thermal Stability and Lifetime of Solid-State Dye-Sensitized Solar Cells via Molecular

Engineering of the Hole-Transporting Material Spiro-OMeTAD. *ACS Appl. Mater. Interfaces* **2015**, *7* (21), 11107–11116.

(42) Schuettfort, T.; Snaith, H. J.; Nish, A.; Nicholas, R. J. Synthesis and Spectroscopic Characterization of Solution Processable Highly Ordered Polythiophene-Carbon Nanotube Nanohybrid Structures. *Nanotechnology* **2010**, *21* (2), 25201.